Progress in Biophysics and Molecular Biology 144 (2019) 151–165

Contents lists available at ScienceDirect

Progress in Biophysics and Molecular Biology

journal homepage: www.elsevier.com/locate/pbiomolbio

Original Research

X-ray diffraction imaging of cardiac cells and tissue

Jan-David Nicolas [a], Marten Bernhardt [a], Susanne F. Schlick [b], Malte Tiburcy [b], Wolfram-Hubertus Zimmermann [b, c], Amara Khan [d, e], Andrea Markus [d], Frauke Alves [d, e], Karl Toischer [f], Tim Salditt [a, *]

[a] Universität Göttingen, Institut für Röntgenphysik, Friedrich-Hund-Platz 1, 37077 Göttingen, Germany
[b] Universitätsmedizin Göttingen, Institut für Pharmakologie und Toxikologie, Robert-Koch-Str. 40, 37075 Göttingen, Germany
[c] DZHK (German Center for Cardiovascular Research), Partner Site Göttingen, Oudenarder Straße 16, 13347 Berlin, Germany
[d] Max-Planck-Institut für Experimentelle Medizin, Hermann-Rein-Straße 3, 37075 Göttingen, Germany
[e] Universitätsmedizin Göttingen, Institut für Diagnostische und Interventionelle Radiologie, Robert-Koch-Str. 40, 37075 Göttingen, Germany
[f] Universitätsmedizin Göttingen, Klinik für Kardiologie und Pneumologie, Robert-Koch-Str. 40, 37075 Göttingen, Germany

ARTICLE INFO

Article history:
Received 20 March 2018
Received in revised form
18 May 2018
Accepted 25 May 2018
Available online 18 June 2018

Keywords:
X-ray diffraction
Cardiomyocytes
Heart muscle
Sarcomere
STED microscopy
Scanning transmission X-ray microscopy

ABSTRACT

With the development of advanced focusing optics for x-rays, we can now use x-ray beams with spot sizes in the micro- or nanometer range to scan cells and large areas of tissues and continuously record the diffraction signals. From this data, x-ray scattering maps or so-called x-ray darkfield images are computed showing how different types of cells or regions of tissues differ in their diffraction intensity. At the same time a diffraction pattern is available for each scan point which encodes the local nano-structure, averaged over many contributing constituents illuminated by the beam. In this work we have exploited these new capabilities of scanning x-ray diffraction to investigate cardiac muscle cells as well as cardiac tissue. We give examples of how cardiac cells, especially living, cultured cells, can be prepared to be compatible with the instrumentation constraints of nano- or micro-diffraction instruments. Furthermore, we show how the developmental stage, ranging from neonatal to adult cells, as well as the final preparation state of the cardiomyocytes influences the recorded scattering signal and how these diffraction signals compare to the structure of a fully developed cardiac muscle.

1. Introduction

Our current understanding of force generation in skeletal and heart muscle is to a large extent based on the structural analysis of the highly ordered acto-myosin assembly in the sarcomere as well as the corresponding structural dynamics, for example under different mechanical loading. Classical x-ray diffraction studies of skeletal (Huxley, 1996) and heart muscle (Matsubara, 1980) have helped to elucidate the basic structure of the sarcomere. In contrast to electron microscopy, an important advantage of x-ray diffraction for the study of muscle structure is the fact that diffraction is compatible with *in situ* recordings under mechanical load, under different physiological parameters, and in parallel to measurements of the contractile force. With the advent of brilliant third generation synchrotron radiation, molecular details of the myosin head dynamics, binding, and stroke have been unraveled in seminal diffraction experiments (Lombardi et al., 2004; Linari et al., 2015; Ait-Mou et al., 2016; Reconditi et al., 2017).

In these experiments, however, structural information is averaged over macroscopically large volumes of the muscle tissue, without any real-space resolution. This classic approach maximizes the signal-to-noise level, but impedes the observation of local structures. Without sufficient real-space resolution, the correspondance between the sarcomeric structure and the cardiac cytoarchitecture is obscured. Yet, we know that the cytoarchitecture shows characteristic variations of fibril orientation, density and histological appearance. One can speculate that these functionally relevant structures on micrometer scales are coupled to corresponding changes at molecular scale. In order to understand the mechanism of force generation beyond average values, mapping of structural variations is required, with real-space resolution down to sub-cellular scales.

Continued progress in x-ray optics has enabled diffraction experiments with spot sizes in the micrometer and even nanometer

* Corresponding author.
E-mail address: tsaldit@gwdg.de (T. Salditt).

https://doi.org/10.1016/j.pbiomolbio.2018.05.012

range (Sakdinawat and Attwood, 2010), well-suited to record the small-angle x-ray scattering (SAXS) of complex soft-matter structures (Lutz-Bueno et al., 2016), biomaterials (Lichtenegger et al., 1999; Fratzl and Weinkamer, 2007), or biological cells with spot sizes smaller than a single organelle (Weinhausen et al., 2012, 2014; Hémonnot and Köster, 2017; Priebe et al., 2014; Wilke et al., 2012; Bernhardt et al., 2016). Recently, we have aimed at resolving the cytoskeletal structure of single cardiomyocyte cells at different preparation states. In particular, we recorded diffraction signals of the state when cells have started to actively contract and striation patterns are observed in fluorescence microscopy images. In corresponding experiments on freeze-dried or fixed cells (Bernhardt et al., 2016; Nicolas et al., 2017a) we have been able to observe sufficiently strong anisotropic diffraction patterns, for example in the case of single cardiomyocytes isolated from neonatal rats. In these experiments the probing x-ray beam was raster scanned over the sample and a scattering pattern was recorded at each scan point. The overall concept of scanning x-ray diffraction in the small-angle regime as applied to cardiac cells and tissue is summarized in Fig. 1. The signal could also be linked to the underlying actin cortex, for example by correlation to fluorescence microscopy using fluorescently labeled actin. At the same time, a clear diffraction signature of a sarcomeric complex was not observed. While the diffraction pattern from amicrometer or sub-micrometer spot is expected to differ in strength, functional form, and resolvable range of momentum transfer (q-range), the absence of any typical muscle diffraction peak was rather obscure. Certainly, the level at which the acto-myosin is expressed in neonatal cells is much smaller than in adult cells (Tiburcy et al., 2011). The fixation and preparation of cells possibly also play a significant role. Finally, the problem of radiation damage is accentuated when concentrating x-ray photons to a small spot size.

All of these issues called for a broader and deeper investigation of cell type, preparation pathway, sample environment, and x-ray optical parameters, which is now provided in the here presented work. While the results provided here are original, the present manuscript also serves as a mini-survey and review of all challenges which we have encountered over the last three years in the application of scanning micro- and nano-beam diffraction to heart muscle cells. We present results obtained for three different types of cells: (i) cardiomyocytes from neonatal rats, (ii) human induced pluripotent stem cells (iPS) differentiated to cardiac muscle cells, and (iii) cardiomyocytes from adult mice. As a benchmark, and for comparison, we also present scanning x-ray diffraction results obtained on heart tissue slices from mouse. This comparison shows that much stronger signal levels can be achieved for tissues than for isolated cells. We also show diffraction signals from engineered heart muscle (EHM), which represents early postnatal human myocardium (Tiburcy et al., 2017). For this overview, we have included data obtained for different preparation and fixation states, from simple freeze-dried to cryogenic vitrification and the alive state, and address the experimental challenge in each case. Finally, we include experimental results on different optical settings from micro-to sub-micro-, and nanometer spot sizes, as well as different synchrotron experiments and optical setups.

Most importantly, we can now demonstrate that for the case of adult cardiomyocytes, diffraction originating from acto-myosin complexes can indeed be observed with micro-beam focusing optics. In this way, sub-cellular resolution is now enabled by microfocus diffraction studies of muscle cells. We expect that extension of the approach presented can shed light on how structural parameters vary within cells and tissues on functionally relevant scales.

The manuscript is organized as follows. Following this introduction, we describe micro- and nano-beam experiments on cells in different preparation states in Sec. 2, covering freeze-dried, cryogenically protected as well as living cell preparations. Then, we outline briefly how the data recorded on cardiac tissue can be used to generate parameter maps that show structural parameters that are specific to the acto-myosin complex. The analysis is extended to studies on adult cardiomyocytes in Sec. 4 and we show how such a study can profit from the correlation with fluorescence microscopy in Sec. 5. The article then closes with a summary and outlook.

2. Different sample preparation states and x-ray optical setups

2.1. Freeze-dried cells

Initial attemps to target single, isolated cells using focused x-radiation used dried cell preparations to prevent radiation damage, or, more precisely, to limit the diffusion of free radicals generated by x-rays. Dried preparations offer secondly the advantage that the prepared samples can be very easily handled and mounted into a standard beamline setup. We have followed this approach and performed initial scanning diffraction studies on freeze-dried cardiomyocytes.

The workflow to freeze-dry cells cultured on a silicon nitride window is described elsewhere (Priebe et al., 2014; Bernhardt et al., 2017) and can be summarized as follows: First, cells were cultured on a coated, 1 μm thick silicon nitride window (Silson Ltd.) with a frame size of typically 5 mm. Then, the cells were chemically fixed in 9% formaldehyde solution (Merck KGaA). Typically, after chemical fixation we permeabilized the cell membrane (0.5% Triton X-100, SigmaAldrich Co. LLC), and specifically labeled f-actin (Phalloidin Alexa 488, Invitrogen) and DNA (Hoechst 33342, Invitrogen) to visualize the actin network as well as the cell nuclei. Right before the plunging process, the window with the cells was washed with triethylammonium acetate salt-free buffer (TEAA, 85.6 mM in H_2O, Merck KGaA). The sample was then blotted using standard blotting paper and plunged into a -195° cold ethane/propane bath for vitrification using a Leica Gridplunger (Leica EM GP, Leica). Finally, the cells were transferred into a cryo vial under liquid nitrogen and transported into a custom-built lyophilisator. Two synchrotron experiments were dedicated to the structure analysis of freeze-dried cells. The experiments took place at the GINIX endstation of the P10 beamline at PETRA III, DESY and the nanofocus endstation of beamline ID13, ESRF. The experimental parameters of the beamline configurations are summarized in Table 1.

Fig. 2 gives an overview on results that can be extracted from the scattering data recorded on freeze-dried cell preparations. Data shown in Fig. 2 (A–D) was recorded at P10 while the remaining data was obtained at beamline ID13. In the preparations described here, the scattering data can be correlated to the fluorescence micrographs recorded prior to freeze-drying. Additional fluorescence micrographs were recorded after the freeze-drying process (data not shown) to verify that the cross-striation visible in the fluorescence signal is preserved, indicating that myofibril structure remained intact. Fig. 2(A) depicts a fluorescence micrograph of multiple cardiac muscle cells with cross-striation. Note, that in this example we have used neonatal rat cardiomyocytes obtained after isolation from young rat as previously used e.g. in (Nicolas et al., 2017a). The cells were isolated following the procedure described in (Rother et al., 2015; Richter et al., 2016). For neonatal rat cardiomyocytes the window was pre-coated with a solution containing fibronectin and gelatine (0.5% fibronectin and 0.08% gelatine in sterile H_2O). In the corresponding darkfield map in Fig. 2(B), nuclei are well contrasted while the myofibril orientation in Fig. 2(C) is extracted from the scattering and can be depicted by color using the

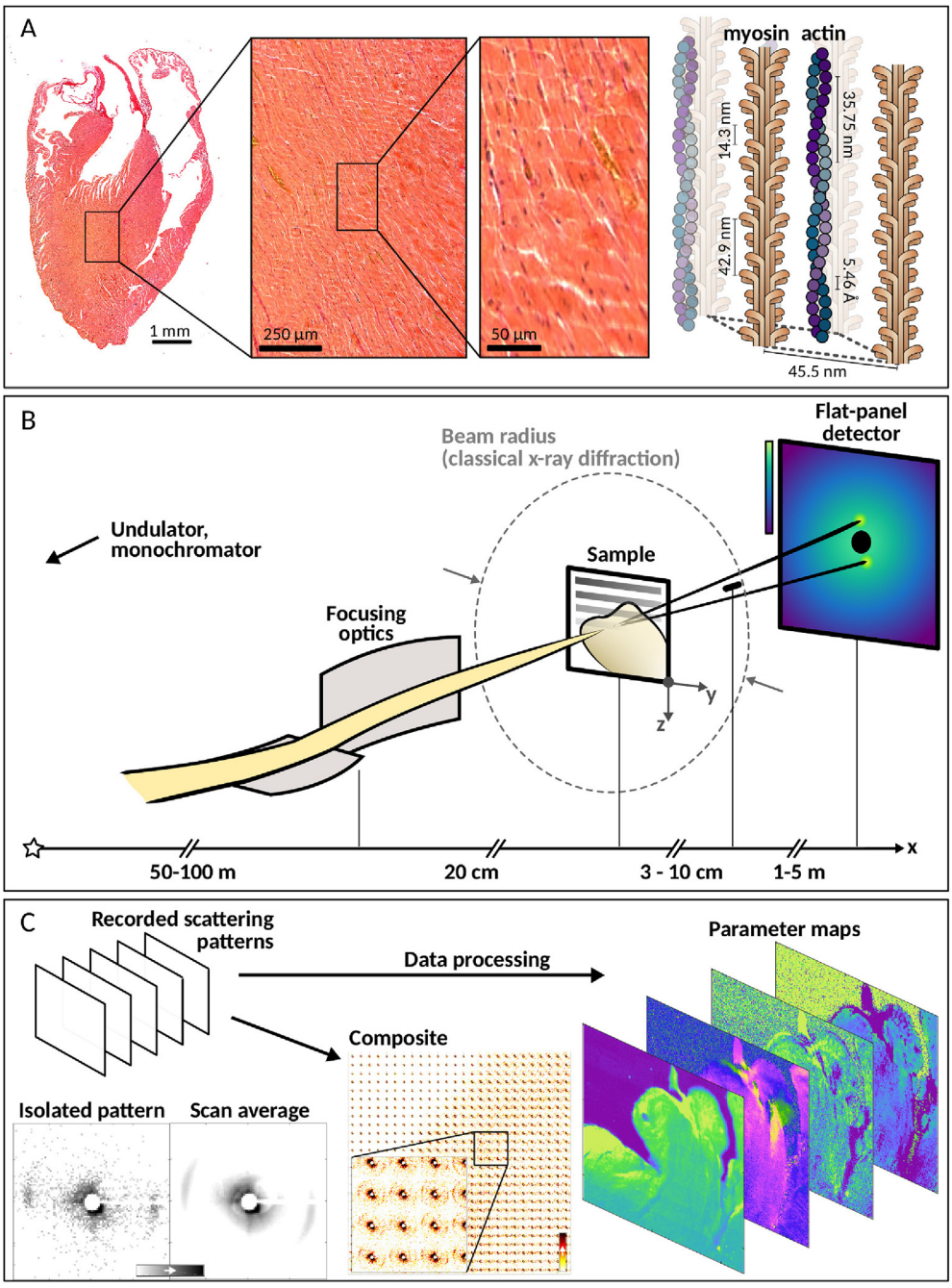

Fig. 1. Experimental concept. (A) Murine cardiac tissue on multiple length scales. (left) A picrosirius red-stained longitudinal heart section together with (center) two different magnifications, and scheme of myosin and actin fibers in an hexagonal arrangement (right). Fundamental helical repeat distances are indicated as well as the unit cell and the lattice constant. (B) Simplified overview of the experimental setup for scanning diffraction studies. X-rays can be focused by e.g. focusing mirrors, the sample is motorized with piezo-electric motors and a single photon counting detector is employed and synchronized to the motor stage for data recording. Further downstream, a small absorber blocks the primary beam to protect the detector and to reduce air scattering. Finer sample features can be mapped with this approach compared to classical diffraction experiments which employ much larger beam diameters. (C) Recorded scattering patterns obtained during a scan can either be reduced to a single scattering pattern or displayed with respect to their scan position. Each scattering pattern can also be analyzed in view of structural features (parameter maps).

cyclic color map design from (Kovesi, 2018). In this representation, the color is representative for the myofibril orientation in the range of $\left[-\frac{\pi}{2},\frac{\pi}{2}\right)$. The corresponding direction of the scattering is rotated by 90°, into the range $[0,\pi)$.

Next, we averaged all scattering patterns from the scan and integrated the resulting image azimuthally. The intensity in this representation is plotted as a function of the wave vector transfer q_r, defined as $q_r = \frac{4\pi}{\lambda}\sin(\theta)$ where λ is the wavelength of the radiation and 2θ is the scattering angle. The index r is used to clarify that we refer to the radial component of the wavevector. The azimuthally integrated curve, also referred to as the one-dimensional structure factor, is shown in Fig. 2(D). At large q_r the structure factor decays according to the power law $I(q_r) \propto q_r^{-c} + d$ where c denotes the Porod exponent and d the noise level of the experiment. Here, we obtained a Porod exponent of $c = 3.9$ from a power-law fit. The importance of the Porod exponent is derived from its property to classify the statistical properties of the

Table 1
Experimental configuration of beamline P10/GINIX, DESY and beamline ID13, ESRF during scanning diffraction experiments on freeze-dried and living iPS cells.

Beamline	P10 (DESY)	ID13 (ESRF)
Energy (keV)	13.8	14.64
Monochromator	Si(111) double cryst.	Si(111) channel-cut mono.
Detector	Pilatus 300k (Dectris)	Eiger 4M (Dectris)
Detector distance (m)	5.12	1.93
Focus (nm^2)	350 × 430	150 × 150
Focusing	Kirkpatrick-Baez mirrors	Compound refractive lenses
I_0 (ph/s)	8.86×10^{11}	9.64×10^{10}
Beamstop	17 × 12 × 0.28 mm^3 Si foil 8 × 7 × 0.025 mm^3 W foil	300 μm diameter, Pb wire

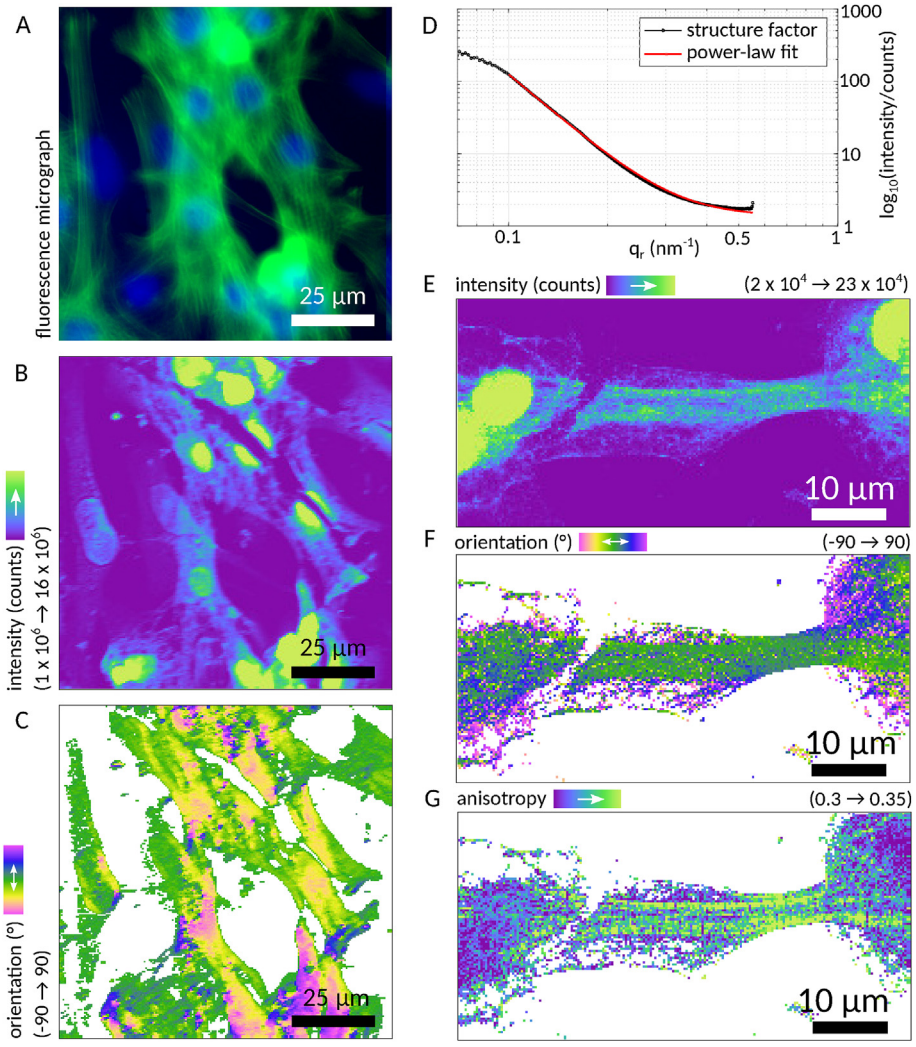

Fig. 2. Fluorescence micrographs, x-ray darkfield and orientation maps on single, freeze-dried cardiomyocytes. (A) Optical image and (B) x-ray darkfield map of neonatal rat cardiomyocytes. (C) Map of the local filament orientation. Scan points with a scattered intensity below 1×10^6 counts were colored white. Note that in regions of very low anisotropy, the orientation is biased towards zero degrees (green). The one-dimensional structure factor obtained after azimuthal integration of the average of all scattering patterns from the scan is shown in (D). The power-law decay can be fitted and a Porod exponent assigned to the structure. (E) X-ray darkfield map of an iPS-derived cardiomyocyte. Once again, the orientation in (F) is obtained by PCA analysis. The anisotropy contrasts more specifically the highly oriented actomyosin filaments. (G) Along the filament axis, the anisotropy appeared modulated. This modulation originated from the striated actomyosin filaments. Scan points in (F–G) with a scattered intensity below 2×10^4 counts were colored white.

underlying structure from which photons are scattered in a very concise and condensed manner. The Porod exponent finds wide spread use in the characterization of structure of macromolecular solutions, suspensions and gels investigated by small-angle x-ray scattering experiments. While it is model independent as such, different models of geometric structure can easily be tested against the measured exponent. Since more recently, the Porod exponent is also used to characterize the more complex cytoskeletal network of cells, see e.g. (Weinhausen et al., 2012, 2014; Priebe et al., 2014; Bernhardt et al., 2016).

The anisotropy of the scattering can inform on how oriented the scattering structure is on average in a given point and in which directions scattering is strongest. For cardiomyocytes the principal directions of the scattering patterns are typically correlated with the local orientation of the actin filaments (Bernhardt et al., 2016). More generally, it reflects the direction and strength of macromolecular polarisation, which is an important descriptor of the local cell structure. Note that the scattering signal is a sum over many different contributors, not just actin alone. The degree to which the scattering is anisotropic is quantified by the unitless anisotropy parameter ω (Bernhardt et al., 2016). Following a principal component analysis (PCA) of the scattering distribution, one can first assign two eigenvectors to each scattering pattern, where the larger eigenvector $\vec{v}_1$ is pointing along the primary scattering direction while the smaller eigenvector $\vec{v}_2$ is orthogonal to $\vec{v}_1$. The filament orientation shown in Fig. 2(C) corresponds to $\vec{v}_2$, based on the fact that scattering from a cylindrical structure extends furthest perpendicular to the main axis. From the corresponding eigenvalues λ_1 and λ_2, which have a meaning in themselves related to the predominant length scale of scatterers respectively, one can compute the unitless anisotropy parameter,

$$\omega = \frac{|\lambda_1 - \lambda_2|}{\lambda_1 + \lambda_2} .$$

This value is confined to the interval $[0, 1]$ where 0 corresponds to a complete isotropic signal and 1 to a perfectly anisotropic, oriented scattering distribution.

In Fig. 2(E–G) we give an example, where the characterization of the anisotropy can be useful. In this example we have used induced pluripotent stem cells (iPS) that were reprogrammed from cells of human gingiva into their pluripotent state and redifferentiated into cardiomyocytes. For a detailed description of this procedure, see e.g. (Tiburcy et al., 2017). For optimal adherence of iPS cells to the silicon nitride membrane, it was coated using Synthemax (0.025 mg/ml; Corning Synthemax II-SC substrate, Merck KGaA) coating solution. Furthermore, iPS cells were chemically fixed in 4% formaldehyde solution (Roti-Histofix 4%, Roth GmbH + Co. KG). The darkfield map is shown in Fig. 2(E). From the orientation map in (F) one can read that the actin filaments run horizontally and the myofibrils can be most specifically visualized in the anisotropy map depicted in (G). Along the myofibrils shown in (G), the anisotropy even appears periodically modulated as one could expect from the cross-striated nature of the fibrils.

One should add that the PCA approach is in certain cases not suitable for the extraction of the orientation and anisotropy of the scattering. Similar results can however be achieved by calculating the circular mean and variance of the one-dimensional intensity profile $I(\phi)$ that has been obtained by radial integration over a certain q_r-range. We suggest to resort to the circular mean and variance if the overall signal is very low and other scattering contributions with a preferred directionality are superimposed onto the signal of interest. An example will be given further below. Note, that the circular variance is defined within $[0, 1]$ as in the case of the anisotropy, only, that a value of 1 now corresponds to a perfectly isotropic signal. Further, note that all analysis routines have been implemented in the nanodiffraction toolbox, described in (Nicolas et al., 2017b) and available from GitHub (https://irpgoe.github.io/nanodiffraction/).

2.2. Micropatterning

So far, order parameters have been deduced but no specific acto-myosin diffraction signal was observed. We have hypothesized that in contrast to fully developed muscle cells, the cytoskeleton of neonatal cells simply does not express the same degree of ordering due to missing mechanosensing cues. Multiple cues can lead to a preferential alignment and ordering of the cells, such as micro-pattering, shear flow or mechanical and electrical stimulation. We have chosen to use micro-patterning as a technique to stimulate the development of aligned myofibers. The sample preparation technique was adapted from protocols in (Shen et al., 2008) and (McDevitt et al., 2002). All experimental parameters of the x-ray experiment are listed in Table 1.

First, a master mold was fabricated. For this purpose, a negative photoresist was spin coated onto a silicon wafer and developed according to a custom design. A 100 nm thin layer of chromium was then deposited and the photo-resist was removed in a lift-off process. The actual grooves could now be etched into the wafer by using reactive ion etching (RIE). The final design of the master mold features 20 μm thin lanes. The depth of the grooves was approximately 10 μm.

To cast a stamp, a polymer (Sylgard 184 silicone elastomer kit, Dow Corning) is mixed with a curing agent (Sylgard 184 silicone elastomer kit, Dow Corning) and poured over the Si master. The stamp is then degassed in a vacuum cabinet for 10 min and baked afterwards for 2 h at 65° C. Then, the PDMS is peeled off the master wafer and cut to an appropriate size for further usage. The stamp is turned upside down and 10 μl to 50 μl fibronectin coating solution is pipetted onto the grooved stamp surface. After 30 min, the stamp is washed three times in phosphate-buffered saline (PBS) and let dry. The stamp can now by carefully placed onto a clean silicon nitride window that was made hydrophilic by means of plasma cleaning for 5 min in a plasma cleaner (Expanded Plasma Cleaner PDC-002, Harrick Inc.). A small weight of 30 mg is added to enhance the transfer of the coating layer onto the silicon nitride. The weight has to be well adjusted to prevent the thin window from breaking. The stamp casting and coating process is summarized in Fig. 3(A).

A fluorescence micrograph proving a successful transfer of the coating layer and culture of iPS-derived cardiomyocytes on the coated lines is shown in Fig. 3(B). We have applied this approach and imaged iPS-derived cardiomyocytes cultured on a micro-patterned surface. An example is shown in Fig. 3(C). The fluorescence micrograph shows that the myofibrils were indeed intact as indicated by the cross-striations of the myofibrils in the fluorescence signal. Even though the micropatterning approach did not lead to a significant increase of the small angle scattering signal, we could observe that the anisotropy map in Fig. 3(E) correlates very well with the fluorescence micrograph in (D), underlining once more that it can represent the degree of alignment of the filaments. From (E) one can even infer that one myofibril is most prominently aligned, indicated by an arrow, while the same statement cannot be made for the fluorescence signal in (D).

2.3. Cryogenic recordings

Following experiments on freeze-dried preparations, it was necessary to test whether this invasive sample preparation procedure had caused the absence of a clear acto-myosin diffraction signature. To test this hypothesis, we have performed scanning diffraction experiments on (i) cryo-protected as well as (ii) vitrified cells. While (i) is simply a means to prevent rapid decay of macromolecular structure after irradiation as in cryo-crystallography, (ii) in addition avoids dehydration artefacts and structural changes already before the x-ray recording. Note that for (ii), the thin water layer surrounding the cells is quasi-instantaneously turned to an amorphous state by rapid plunge freezing (vitrification), and cells are covered by this vitreous layer at all times. The native structure is thus preserved, unless flaws in the handling and the sample transfer result in ice formation when the

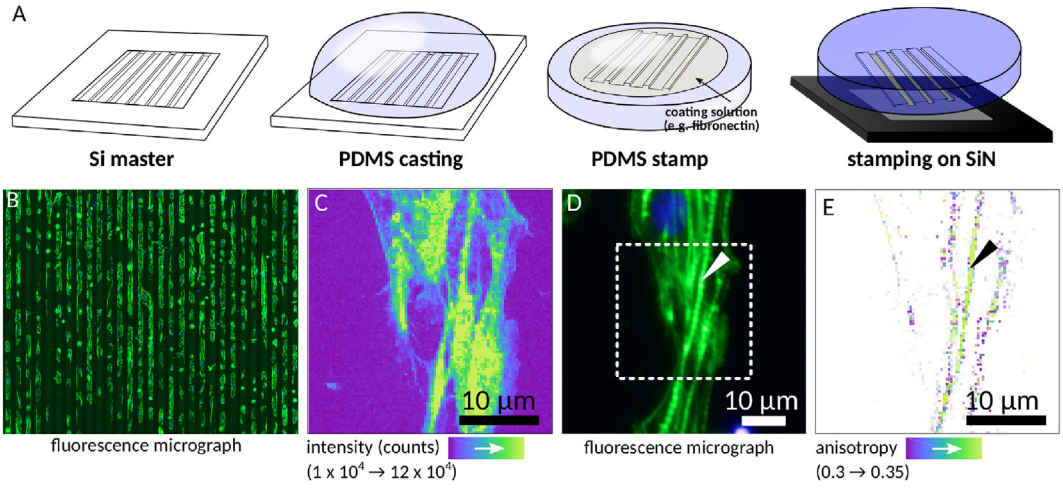

Fig. 3. Microcontact printing. (A) Preparation of PDMS stamps for micropatterning. Grooves of 20 µm width and 10 µm height were etched into the silicon wafer using reactive ion etching. PDMS was cast over the silicon master. The PDMS stamp was cut into the desired size and shape and the flat side is coated with fibronectin coating solution. Finally, the stamp could be used for transferring the fibronectin coating onto the silicon nitride window. A weight was usually placed onto the PDMS stamp to transfer the coating evenly onto the substrate. Fluorescently labeled actin filaments of iPS-derived cardiomyocytes cultured onto micropatterned substrates are shown in (B). Note that cardiomyocytes attached only to the stamped fibronectin lines. (C) Darkfield map of iPS-derived cardiomyocytes on a micropatterned window. Striation of the fibrils was observed in the micrograph in (D). The most strongly aligned myofiber, indicated by an arrow in (D) and (E), can be found by referring to the anisotropy map in (E). Here, background was removed from the graphic by additionally scaling the color from white to fully saturated within the range 0.3 (white) to 0.35 (saturated).

temperature rises above the glass point. The fact that the rapid cooling rate indeed 'fixes' macromolecular structures is very well established from electron microscopy. For both cases, (i) and (ii), the cryogenic temperature during the x-ray recording increases the window of tolerable x-ray dose, and hence also the possibility to detect weak signals. For (i), the sample should ideally be free of water. Here, we have used freeze-dried cell preparations for this purpose, and have inserted them into a cold nitrogen gas stream ($T \approx 170$ K). Vitrified samples have to be kept at cryogenic temperatures at all times, either by mounting the sample onto a cold finger and inserting the sample into a vacuum chamber, or by rapid mounting of the sample into a cold nitrogen gas stream. Cryogenic chambers for x-ray experiments on vitrified samples have been described before (Nakasako et al.; Chen et al., 2014; Hitchcock, 2015) but are highly specialized developments with limited access and flexibility, even though the demand for such developments is currently rising (Yusuf et al., 2017; Meisburger et al., 2013; de Jonge et al., 2014).

In the following, we describe experiments using an N_2 Cryostream (Oxford Cryosystems). The general workflow was described earlier (Priebe et al., 2014) and can be summarized as follows: First, cells are cultured on a 1 µm thick silicon nitride window with a frame size of typically 5 mm. In this case, the frame size is chosen such that it fits the cryogenic stream of approximately 7 mm diameter. The samples are then vitrified as in the case of freeze-dried preparations and stored in cryovials under liquid nitrogen until right before the experiment.

The preparation at the beamline consists of four steps, see Fig. 4(A–E). First, a cryovial is opened and the window is placed into the groove of a metal block to facilitate mounting the sample into the magnetic sample holder. The window is then gently moved into the opening slit of the sample mount. Once inserted, the sample is fixed by a screw. The magnetic sample mount is then once again covered by a plastic vial that is attached magnetically to the mount. So far, all steps were conducted under liquid nitrogen. The sample is now prepared to be taken to the experiment, where the cryostream is put in place and operating. Placing the sample into the cryostream without exposing it to room temperature is crucial and the bottleneck in the sample processing queue. We typically proceeded by taking the vial with the sample out of the cryobath and placing it onto the magnetic mount of the sample tower. At this point, the vial should still contain liquid nitrogen. Then, the sample typically needed to be quickly rotated such that the sample surface is parallel to the stream direction and the cover is removed as fast as possible to avoid potential heating. The final arrangement is shown in Fig. 4(F).

Fig. 4(G) shows the x-ray darkfield map of cryoprotected iPS derived cardiomyocytes which are bridging two fibronectin-coated lines. The corresponding fluorescence image recorded prior to freeze-drying is shown in Fig. 4(H). The background in (G) has a grainy structure stemming from ice crystals due to water adsorption at the cold sample surface. After approximately 1 h of experiment time, we have observed ice crystal formation (I) at the center of the silicon nitride window. During the course of this experiment, ice crystal formation was very difficult to prevent, possibly due to the fact that the cold N_2 stream was not perfectly shielded by a coating of dry N_2 atmosphere. Fig. 4(K) shows a sample of vitrified iPS-derived cardiomyocytes on a homogeneously coated silicon nitride surface. In this particular case, we could observe the vitrified water layer in the beamline's on-axis optical microscope. Again, the iPS-derived cardiomyocytes can be recognized in the x-ray darkfield. In this case, the background exhibits a 'network-like' pattern. Based on the diffraction signal, it became apparent that intensity in the background was caused by ice cracks which exhibited strongly anisotropic and modulated diffraction signals. The vitrified iPS-derived cardiomyocytes give rise to predominantly isotropic scattering, and with no sign of any particular ordered acto-myosin structure such as in muscle.

The experiments also illustrate well which technical challenges are still associated with scanning x-ray diffraction of cells. This is even more the case for studies of living cells, as reported in the next section.

2.4. Living cells

For living cells, the strategy must be opposite to cryogenic recordings. Instead of 'freezing' the structure and rendering it more 'radiation resistant', one must now try to outrun radiation damage

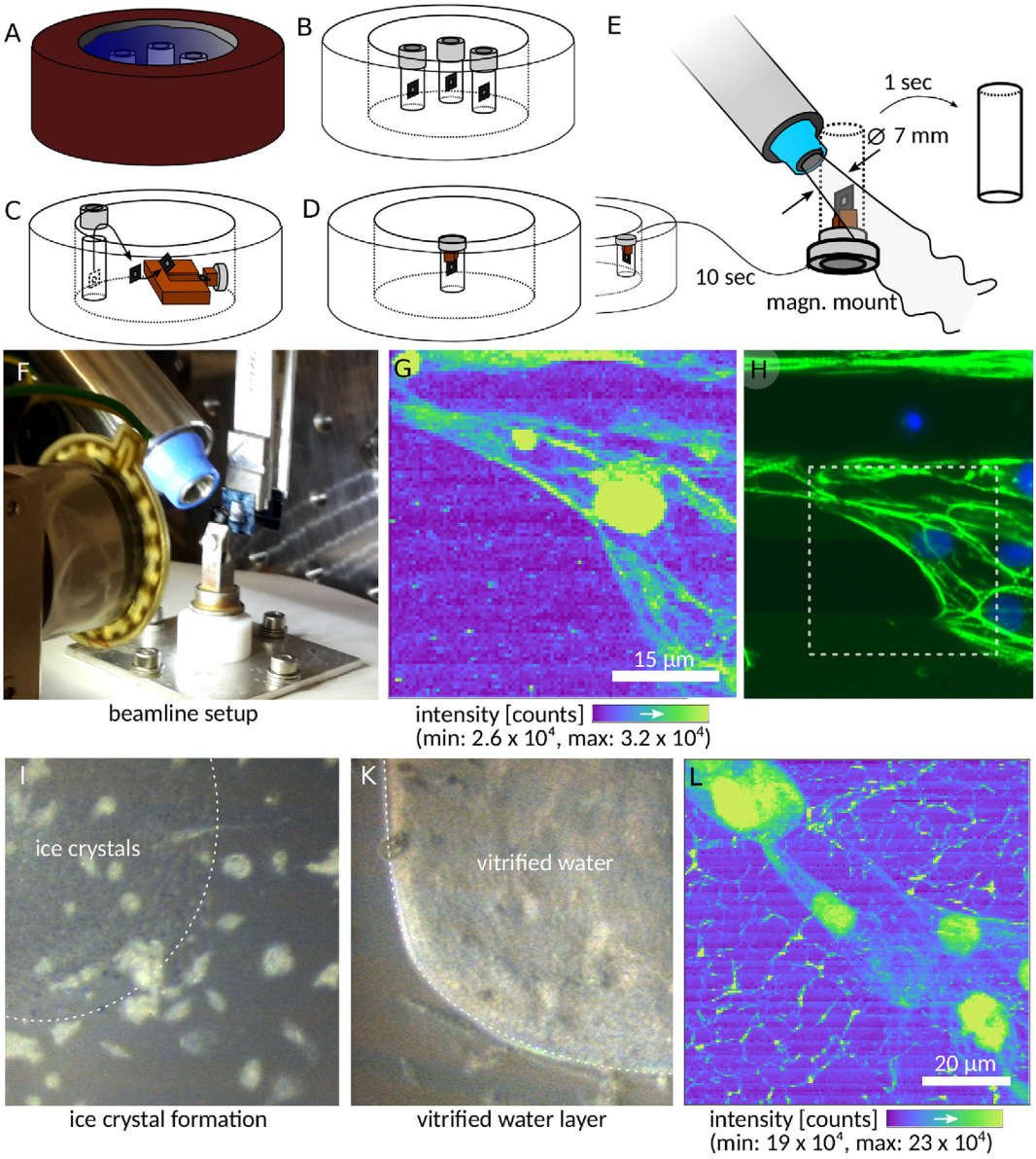

Fig. 4. Cryopreservation in scanning x-ray diffraction experiments. (A–F) Mounting of the sample into the beamline setup. (A) Dewar with vials, (B) 'x-ray vision' sketch, (C) mounting of the sample into the sample holder under liquid nitrogen, (D) prepared sample on magnetic mount, (E) mounting the sample onto the motorized stage into the cryostream. The cap has to be removed quickly in order to prevent thawing of the sample. (F) Photograph of the mounted sample. (G) Darkfield contrast map of a freeze-dried cardiomyocyte, cryoprotected using a cryostream. (H) Fluorescence micrograph with a white dashed box indicating the area corresponding to the scanned region in (G). After several minutes, ice crystals started to form on the silicon nitride membrane, as can be seen in (I). A mounted, vitrified sample is shown in (K) and the corresponding darkfield map shown in (L).

in time by very quick shots, each on pristine sample regions. Dose rate becomes the key quantity, not just dose, and scan points must hence be spaced sufficiently wide. The extreme case of such a 'diffract before destroy' principle has turned into reality by the development of free-electron laser (FEL) radiation sources, which are uniquely suited to target the living state of biological matter (Ekeberg et al., 2015; Seibert et al., 2010; Hantke et al., 2014; Kimura et al., 2014). From a preparation point of view, living samples do not require processing and are hence easier to prepare. However, the accurate design of sophisticated x-ray compatible sample chambers requires great care. In this respect, three basic concepts are generally followed: (i) static chambers that typically consist of two windows glued together and containing a small, microliter-sized amount of liquid ,see e.g. (Strelnikova et al., 2017), (ii) microfluidic chambers (Denz et al., 2018; Ghazal et al., 2016), and (iii) jet or droplet injection systems (van der Schot et al., 2015).

Here, we describe the use of a static chamber for scanning diffraction experiments with the possibility to extend the chamber design to microfluidic applications. The chamber set was purchased from Silson (Silson Ltd.). It consists of two opposing silicon nitride windows. A polymer spacer is deposited on one window. Since the height of the SU8 spacer material can be very accurately controlled in the manufacturing process, the overall height of the water layer can be adapted to the sample under consideration. Here, we have chosen a spacer thickness of 70 µm and 100 µm to accomodate the cells and leave a remaining sufficiently large volume so that products of metabolism do not accumulate too rapidly. The cells, in this case iPS-derived cardiomyocytes, are cultured for 3–7 days on the window without the polymer spacer. The chamber is then closed by carefully placing the window containing the polymer

spacer onto its counterpart. To tightly seal the chamber, it is inserted between two aluminium frames that are carefully screwed together. The assembled chamber can then be inserted into a sample holding pin. The overall design of the chamber is shown in Fig. 5(A). This design was tested during two consecutive beamtimes at beamline P10 (GINIX endstation), DESY and ID13, ESRF.

The experimental parameters for both experiments are summarized in Table 1 (ID13) and Table 2 (P10). In both experiments, we have used iPS-derived cardiomyocytes. Fig. 5(b) shows a darkfield map of a dense population of iPS derived cardiomyocytes in their liquid environment. The radiotoxic effect on the cells was most easily verified by later visual inspection of the cells in an optical stereo microscope available at the nearby safety level 2 laboratory of the Biomedical Facility at the ESRF, as shown in Fig. 5(c). Two scanned regions are clearly visible due to the apparent lack of cells. Interestingly, we found in this example that the adjacent cells were still actively contracting, hereby confirming that the chamber design is indeed well suited for x-ray experiments.

The average of all scattering patterns is shown in Fig. 5(D). The isotropic scattering can be summarized in the one-dimensional structure factor. The azimuthally integrated structure factor of a single scattering pattern, is shown in Fig. 5(E). The power-law fit resulted in a value of $c = 3.0$ for the Porod exponent.

In the experiment at the Göttingen nanofocus setup (GINIX endstation) of beamline P10, cells were not as densely populated as in the previous case. Isolated cells can be very well seen in the darkfield image in Fig. 5(F), however, from their shape one can infer that the cells are already in an apoptotic or necrotic state. Re-inspecting the cell chamber under the optical microscope confirmed this assumption. It is not surprising that radiation damage progressed faster than the scan area could be covered. For this reason, we recorded scattering patterns at isolated locations that were not yet exposed to x-rays (data not shown). Such patterns were again predominantly isotropic, which gave additional evidence that myofibrils in iPS-derived cardiomyocytes are not as well ordered on the nanoscale as one might expect based on the striation pattern observed in fluorescence micrographs, and the ability of the cells to contract.

Table 2
Experimental configuration of beamline P10/GINIX, DESY during scanning diffraction experiments on cryoprotected and vitrified cells.

Beamline	P10 (DESY)
Energy (keV)	13.8
Monochromator	Si(111) double cryst.
Detector	Eiger 4M
Detector distance (m)	5.12
Focus (nm^2)	309×301
Focusing	Kirkpatrick-Baez mirrors
I_0 (ph/s)	7.75×10^{10}
Beamstop (mm^2)	10×7, 0.2 mm thick Cu foil

3. Cardiac tissue

All cell preparations presented thus far made use of cardiomyocytes either from neonatal rats or human iPS cells as indicated, which allowed for culturing of the cells on silicon nitride windows. We showed here that multiple structural parameters can be extracted from the small-angle scattering signal. However, modulations of the scattering, either originating from the filament arrangement in an hexagonal lattice or from helical repeats of the

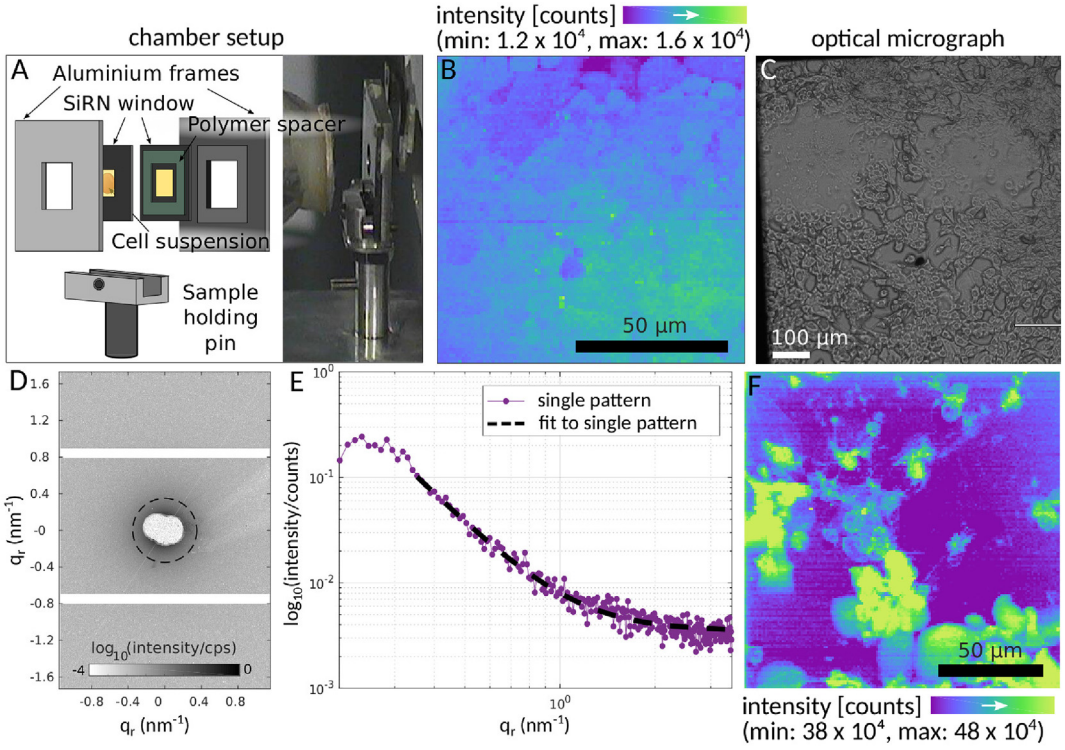

Fig. 5. Scanning x-ray diffraction on living iPS-derived cardiomyocytes. (A) Sketch and optical image of the assembled static chamber for experiments on living cell cultures. Two silicon nitride windows were sandwiched between two aluminium holders and tightly sealed to avoid leakage. (B) Darkfield map of a dense population of cells in the liquid chamber recorded at beamline ID13, ESRF. (C) Optical micrograph recorded with a stereomicroscope after the x-ray experiment was performed. Damage due to the intense x-ray beam led to cell death in the scanned areas. Cells from non-exposed areas were still contracting. (D) Average scattering pattern obtained from the scan in (B). A Porod fit to the structure factor decay of an isolated pattern is shown in (E) with a Porod exponent of 3.0. (F) Darkfield map of a less dense population of cells obtained from an experiment at beamline P10/GINIX, DESY.

myosin or actin filaments, was lacking. We hypothesized that the invasive sample preparation in the case of freeze-dried cells, even when aligned by micropatterning, might be the leading cause for the absence of layer lines, i.e. interference from the helical assembly of the filament subunits, or interfilament interference. However, due to the fact that the interfilament interference was not present in the case of living and vitrified cells, we conclude that due to the immaturity of the cardiomyocytes cultured in 2D sarcomeric structure is simply not yet fully developed. We therefore conducted a scanning diffraction study on cardiac tissue to verify that in histological sections of an healthy, adult mouse heart, modulations stemming from interfilament interference can be detected. The samples were mounted between two polypropylene foils as described in (Nicolas et al., 2017b). Key experimental parameters are summarized in Table 3(left).

Indeed, Fig. 6(A) shows a scattering pattern and a map of multiple averaged scattering patterns obtained on heart muscle tissue obtained from adult mouse. The interfilament interference, i.e. the (1,0) and (1,1) reflections, can be clearly seen together with the directionality and anisotropy of the scattering signal. Note, that these reflections stem from the hexagonal array of filaments in the A-band of the sarcomere. The interplanar spacing $d^{(1,0)}$ is related to the reflection position $q_r^{(1,0)}$ by $d^{(1,0)} = \frac{2\pi}{q_r^{(1,0)}}$. In turn, the (1,1) reflection position is obtained by $q_r^{(1,1)} = \sqrt{3} q_r^{(1,0)}$. Lastly, the lattice constant a is identical to the spacing of the myosin filaments and is given by $a = 2d^{(1,0)}/\sqrt{3}$. In the following maps, we report the (1,0) reflection position $q_r^{(1,0)}$. To generate e.g. the darkfield map shown in Fig. 6(B), we have used a 'stitching mode' to scan the tissue: Since the scanning range of the piezo motor used for continuous scanning of the sample could only cover an area of 200 × 200 μm^2, multiple scans (patches) were performed at adjacent locations with exactly 0% overlap and consisting of 26 × 26 scan points per patch. The darkfield map is generated by displaying all patches next to each other in the appropriate ordering. The tiling grid is superimposed onto the darkfield map for clarity. Note, that Fig. 6(A) was also generated in this fashion, only, that in this case an average scattering pattern from each patch was calculated.

In a straight forward manner, we could now compute the orientation and anisotropy map as shown in Fig. 6(C–D), as well as a map of the (1,0) reflection position. Note, that background is colored in white in Fig. 6(D–E), identified by a darkfield intensity below 700 counts. As we have reported in an earlier study on cardiac tissue (Nicolas et al., 2017b) and contrary to our initial expectation, the reflection position is not constant throughout the tissue but varies continuously within 0.14 nm^{-1} to 0.17 nm^{-1} corresponding to a lattice spacing $d^{(1,0)}$ ranging from 37.0 nm to 44.9 nm. In the literature lattice spacings between 35.0 nm and 38.3 nm are reported for intact, relaxed rat myocardium (Ait-Mou et al., 2016; Irving et al., 2000). To this point a comparison is obscured by the fact that cells and tissue in the preparations used here were chemically fixed and the sarcomere length could not be simultaneously recorded which would be necessary as the lattice spacing is found to vary strongly with sarcomere length (Irving et al., 2000). Once again, we found that the reflection position $q_r^{(1,0)}$ decreases close to the left ventricle of the heart. It was in this case obtained by azimuthally integrating every scattering pattern and fitting a model function of the form

$$I(q_r) = a q_r^{-b} + c \cdot \exp\left(-(q_r - d)^2 \big/ \sigma^2 \right) + e \cdot \exp\left(-(q_r - f)^2 \big/ \sigma^2 \right) + g \,,$$

to the structure factor. In this model, a-g are fit parameters. Here, both reflections are modeled as Gaussians with positions d and f. The reflection width was fixed at $\sigma = 0.034$ nm^{-1} during the fitting process.

Based on such maps, it is now possible to correlate such information to other modalities. This will be of particular importance if one aims at combining the information from scanning x-ray scattering recordings of the type presented in Fig. 6 with histology and immunohistochemistry in a bio-medical setting.

A similar analysis can now be performed on engineered heart muscle (EHM). The experimental parameters for this experiment are given in Table 3(right). The protocol for the preparation of EHM is described in (Tiburcy et al., 2017). Here, we have used circularly shaped EHM. The tissue was chemically fixed after 12 culture days in 4% formaldehyde solution and embedded in an agarose block for sectioning in a vibratome (VT1000 S, Leica Biosystems). Sections were cut to a thickness of 30 μm and sandwiched between polypropylene foils with a small volume of excess PBS to keep the sample hydrated.

The darkfield map of EHM is shown in Fig. 6(F) together with the corresponding average scattering pattern shown in (G). The darkfield map represents the tissue morphology which appears to be dominated by the collagen matrix, while modulations in the scattering patterns were absent. Since the muscle to matrix ratio in EHM is much smaller in comparison to bona fide heart muscle, the absence of sarcomeric reflections can be explained by the very low amount of myofibers in the scattering volume and a muscle diffraction signal is therefore simply not detected. Alternatively, since the cardiac tissue is composed of iPS-derived cardiomyocytes that have only been cultured for 12 days, the sarcomere might be far from exhibiting the long range order known from the 'adult' stage due to the immaturity of the cardiomyocytes. Further research and improved protocols for in tissue imaging are required to safely deduce how well, at the individual sarcomere level, the structure of EHM is developed in comparison to adult heart muscle.

4. Adult cardiac muscle cells

Based on the fact that myofibers in adult tissue give rise to a

Table 3
Experimental configuration of beamline P10/GINIX, DESY. Left: Parameters of the scanning diffraction experiments on adult mouse heart muscle as well as isolated, adult cardiomyocytes. Right: Parameters for the scans performed on engineered heart muscle.

Beamline	P10 (DESY)	P10 (DESY)
Energy (keV)	13.8	13.8
Monochromator	Si(111) channel-cut mono.	Si(111) channel-cut mono.
Detector	Eiger 4M	Eiger 4M
Detector distance (m)	5.05	5.05
Focus (μm^2)	2.3 × 2.3	2.3 × 2.3
Focusing	Compound refractive lenses	Compound refractive lenses
I_0 (ph/s)	0.86×10^{10}	4.08×10^{10}
Beamstop (mm^2)	3 mm diameter, W wire 0.1 mm diameter, W wire	3 mm diameter, W wire 0.1 mm diameter, W wire

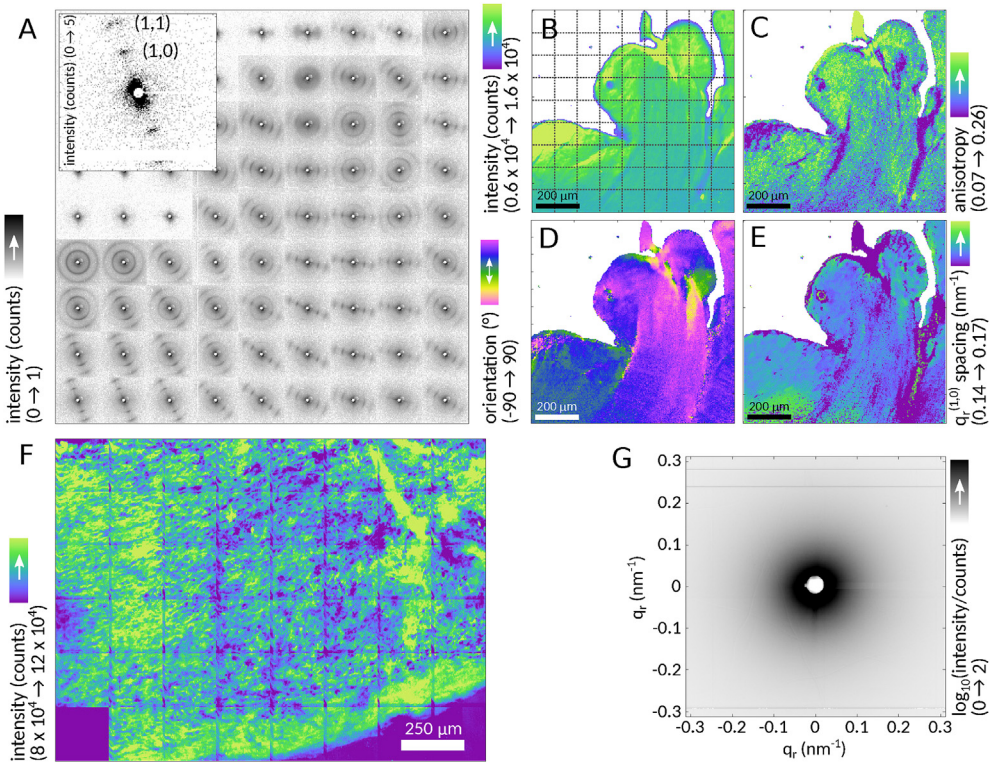

Fig. 6. Scanning x-ray diffraction on cardiac tissue. A section of heart muscle from an adult mouse was scanned and is shown in multiple contrast based on four different structural parameters extracted from the scattering distributions. (A) The entire image was recorded piecewise in 'stiching mode', such that small rectangular regions (fields) were scanned on a cartesian grid. Here, the fields were recorded with exactly 0% overlap. The average diffraction pattern of each field is shown in a composite image together with the scattering pattern from a single location. In (B) the darkfield map is shown and superimposed by the stitching grid for illustration. (C–E) Besides anisotropy and orientation of the scattering as in the case of the cell experiments, the (1,0) reflections allowed for the extraction of the lattice constant of the hexagonal lattice of the actomyosin. In (B–E) pixels with a darkfield intensity below 700 counts have been masked in white. (F) Darkfield map of a 30 µm thick engineered heart muscle (EHM), primarily depicting the collagen matrix. Scattering was dominantly isotropic and unlike the case of the adult cardiac tissue, reflections were not observed. The corresponding average scattering pattern is shown in (G).

specific acto-myosin signal that can be extracted from fits of model functions, it should in principle be possible to extract this signal from isolated single cells that were extracted from adult cardiac tissue. For experiments that were conducted at the GINIX endstation of beamline P10, we isolated cardiomyocytes from hearts of helthy adult mice as well as mice that developed heart fibrosis. As a model system for cardiac hypertrophy and fibrosis, we used TAC-operated (transverse aortic constriction) mice (deAlmeida et al., 2010). In this procedure, mice undergo a surgical procedure where the aorta is constricted by a small thread. TAC treated mice develop cardiac fibrosis after several weeks, which is characterized by an excessive deposition of collagen and other extracellular matrix proteins. We could hereby not only verify that the interfilament interference can be detected as in the case of tissue sections, as shown in Fig. 7(A), but also compare the internal structure of cardiomyocytes from healthy and diseased heart. Cells were isolated from the heart following the procedure described in (Toischer et al., 2010).

For a thorough comparison, single cardiac cells were isolated from adult mice that have been (i) untreated, (ii) sham operated, and (iii) TAC-operated. In all cases, cells were chemically fixed immediately after the extraction from the tissue for conservation and to preserve the cellular structure until the experiment. For the experiments, once again a polypropylene chamber as in (Nicolas et al., 2017b) was used: A small volume of cell suspension of around 30 µl was pipetted onto a polypropylene window and a second window was placed on top. The chamber was sealed using nail polish to prevent drying of the cell suspension. To rule out any effect of the chemical fixative on the filament spacing and the expected scattering signal itself from the fixative used, we employed three different fixation solutions in all three heart preparations, namely 4% formaldehyde (FA) solution, 9% formaldehyde solution, and Karlsson-Schultz (K&S) fixation solution (Karlsson and Schultz, 1965; Schultz and Karlsson, 1965) containing 4% formaldehyde and 2.5% glutaraldehyde. The absolute number of cells that were analyzed with respect to the original treatment of the heart and the chemical agent used for fixation is summarized in Table 4.

In Fig. 7(A) we show one example of an optical micrograph of an adult cardiomyocyte, in this case extracted from a TAC heart and chemically fixed using the K&S fixative solution. In contrast to cultured neonatal cardiomyocytes, adult cardiomyocytes have the commonly observed rod-shape. As expected, the scattering signal from such isolated cells was now similar to the scattering from adult cardiac tissue, even though the signal at a single location was much weaker. The corresponding average diffraction pattern (300 patterns, without background signal) and an isolated diffraction pattern shows the (1,0) reflection in (B). This made it possible to perform a complete analysis of the diffraction signal as in the case of the tissue. In all cases, the scattered intensity, myofibril spacing, and the orientation could clearly be determined, as depicted in Fig. 7(C),(D) and (E), respectively. In these maps, pixels with a darkfield intensity below 200 counts corresponding to background signal are masked in white. Due to the low signal levels, we have now resorted to the circular mean of the azimuthal intensity distribution as a measure for the filament orientation. Interestingly, the (1,0) reflection position was varying significantly from cell to cell, while within a single cell it appeared rather constant

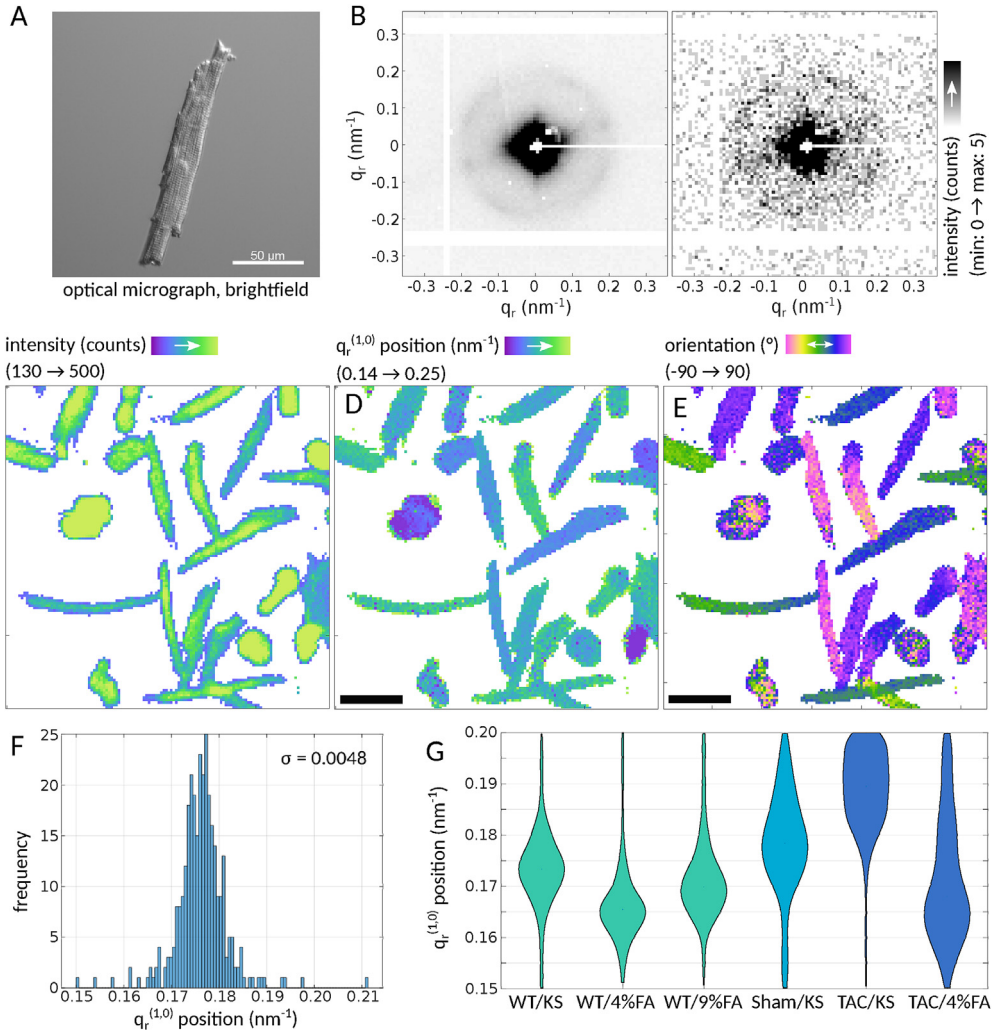

Fig. 7. X-ray structure analysis on isolated adult cardiomyocytes. (A) Optical micrograph of an adult cardiomyocyte. One example for an averaged and an isolated diffraction pattern from such a cell is shown in (B) and (C), respectively. (C) A darkfield map of isolated, hydrated, chemically fixed cells. (D) Position of the (1,0) reflection and (E) filament orientation could be determined pixelwise. Note, that in (C–E), pixels with a darkfield intensity below 200 counts have been masked in white. Note, that the (1,0) position in (D) is not constant but can fluctuate from cell to cell around a mean $q_r^{(1,0)}$ by $\sigma = 0.0048$ nm^{-1} as shown in (F) for the distribution of $q_r^{(1,0)}$ of the cell marked by in asterisk in (D). (G) Different fixation solutions as well as different (patho)physiological conditions of the heart correspond to different filament periods. The distributions of the (1,0) reflection positions of all cells from a certain preparation pathway are represented here as violin plots. Note, that the number of cells that were used for a given preparation pathway is summarized in Table 4.

Table 4
Number of cells analyzed based on preceding mouse treatment and chemical fixative used.

		Fixative		
		9% FA	4% FA	K&S
Treatment	none	10	12	5
	sham	–	–	11
	TAC	–	6	16

throughout, see Fig. 7(F) for a histogram of the (1,0) reflection position obtained from the cell marked by an asterisk in Fig. 7(D).

To quantify the influence of the chemical fixation and mice treatment, in (G) we show violin plots, i.e. normalized, symmetric vertical histograms, of the (1,0) reflection positions of the myofibers respective treatment and fixation. From (G) it becomes apparent, that even though the (1,0) position within an isolated cell is rather constant, the reflection position from the population (cf. Table 4), as we have seen previously in (F) can vary more strongly. In (G) the lattice spacing varies between 0.15 nm^{-1} and 0.20 nm^{-1} or in terms of $d^{(1,0)}$ between 31.4 nm and 41.9 nm. It appears that the greatest difference is between the cardiomyocytes from TAC-treated mice that have been chemically fixed with K&S and FA solution. This may reflect the pathological changes in this model which for example include calcium overload, which may lead to a variable hypercontractile state upon fixation. The results shown in (G) are intriguing since the filament spacing and its distribution in an ensemble of cells might be potentially useful as a biomarker in comparative studies on cardiac diseases. At this point, however, the data obtained in this study does not yet conclusively show that the filament spacing is in fact an indicator for fibrosis. In addition, all fixation solutions employed here can in principle induce shrinkage. If one assumes isotropic shrinkage, then stronger crosslinking would induce smaller lattice spacings which is supported by the data shown in Fig. 7(G). However, a phosphate buffer was used in all fixation solutions, hence, relative changes inferred from Fig. 7(G) should still occur due to the cell model and not the fixation solution. Future experiments are required to clarify the influence of sample preparation on the filament spacing observed in such an

experiment. Furthermore, the cells in this study were extracted from entire hearts which removes any local dependence. Since scanning diffraction maps of cardiac tissue shown here and in (Nicolas et al., 2017b) have already shown that the filament spacing can vary locally within a similar range, one would have to use cells obtained from a specific location in the heart.

It is worth pointing out that the results presented in Sec. 3 and 4 where obtained using a micro-focused rather than a nano-focused beam. This relaxed focusing made it possible to image cardiac tissue and isolated cardiomyocytes at still moderate resolution while reducing the effective dose by approximately two orders of magnitude. This change was especially crucial for the case of adult cardiomyocytes where severe radiation damage by a nanofocused beam could potentially lead to structure degradation within a single exposure and would therefore inhibit the observation of interfilament reflections.

5. Correlative microscopy

Thus far we have exploited the $(1,1)$ and $(1,0)$ reflections as a structural observable that precisely reports on the order, disorder and packing of the filament lattice in the sarcomere. The real-space resolution in the scanning diffraction studies reported above was however limited by the moderate focusing required to avoid artefacts stemming from radiation damage. Incidentially, another means to specifically target the acto-myosin structure is by fluorescent labels. Using state-of-the-art fluorescence microscopy techniques such as confocal microscopy or super-resolution microscopy such as STED enables a very high spatial resolution down to the resolution range that can be accessed by means of scanning diffraction. In this respect, the limited real-space resolution in scanning diffraction can be extended by at least one order of magnitude when fluorescence micrographs of the same structure are recorded.

Such a combination of techniques can be particularly fruitful when the signal is originating from different sources, e.g. the fluorescently labeled cytoskeleton in the confocal or STED micrograph and the total scattered intensity reflecting Fourier components of the complete electron density of the sample. In this case, fluorescence microscopy can benefit from x-ray techniques which directly probe the electron density and thereby offer a highly quantitative contrast mechanism sensitive to the ensemble of biomolecular constituents.

Recently, we have introduced a novel approach of parallel STED or confocal microscopy recordings together with x-ray scanning diffraction and x-ray holography, all integrated into a single synchrotron endstation (Bernhardt et al., 2018). Here we have made use of this setup to image adult cardiomyocytes. For instrumental simplicity and avoiding the technical challenges associated with chamber construction, we have used freeze-dried preparations as a first step. To this end, adult cardiomyocytes were deposited onto a silicon nitride window and fluorescently labeled using the STED-compatible dye Atto633 (AD 633-8X, Atto-tec), followed by freeze-drying.

Fig. 8(A) shows a confocal stack of an isolated cardiomyocyte. In this case, we have not exploited the full STED-capability of the setup since recording an entire STED-stack of a cell would have greatly exceeded the available recording time. Fig. 8(B) shows a single confocal image from the stack, the average image and the maximum projection of the fluorescence intensity throughout the stack. The maximum projection hereby maps the maximum intensity that was recorded in a scan point in all frames for all scan points. The stack average appears rather blurry, while the striated myofibrils are most clearly visible from the single image. Following the confocal recording, we have moved the sample into the focus of the x-ray beam and scanned the sample through the focus position. For this experiment, the experimental parameters are given in Table 5. The darkfield image depicted in Fig. 8(C) is now a map of all cellular components that were traversed by the x-ray beam. The anisotropic scattering due to the aligned myofibrils is apparent from the example scattering pattern shown in Fig. 8(D, top-left). For completeness, we have added the average intensity (D, top-right), maximum projection (D, bottom-left) and the background intensity (D, bottom-right).

6. Summary and synopsis

In summary, we have developed, adapted and evaluated experimental tools for applying micro- and nanofocused hard x-rays to studies of cardiac cells and tissues. This includes beamline instrumentation, comparison of sample preparation and sample chambers, experimental controls, establishing dose limits, monitoring of radiation damage and automated data analysis. A main purpose of this study was to investigate how the x-ray scattering parameters and darkfield images differ in cardiomyocytes of different levels of maturity (lowest level in iPS-derived cardiomyocytes; highest level in cardiomyocytes from adult mice), and how this can be delineated from effects of sample preparation (cells vs. tissue) and experimental parameters (fixatives and cardiomyocytes from healthy and diseased heart). We have described as accurately as possible not only the approaches 'which worked best', but all configurations which were screened and tested. This is for two reasons. First, the work is still primarily method driven, and technical aspects, developments and parameters including the 'does', 'don'ts' should be clearly specified. Secondly, the absence of signal in many of the experiments are indeed the message. Precisely the fact that the highly structured diffraction pattern of classical muscle diffraction was lacking in monolayer cultures of immature cardiomyocytes and engineered heart muscle from iPS-derived cardiomyocytes, is the lesson learned.

In particular, we found that both for single cardiac cells as well as for tissue, cardiomyocytes from neonatal rats and derived from iPS cells do not give rise to interfilament interference or layer lines. The same was true for engineered tissue. The use of micropatterning for freeze-dried cells and the embedding of cardiomyocytes in a collagen matrix did lead to an alignment of cardiomyocytes in 2d and 3d, respectively, but not to a more ordered internal structure on the level of the sarcomere. In all cases but the adult cardiac cells and tissues, reflections were not detected. This finding can be explained by a poor sarcomere organization, a loss of signal due to a too small number of myofibers in the scattering volume in the case of 2d monolayers of cardiomyocytes, or a blurring of scattering images due to an overlay by highly abundant isotropically organized extracellular matrix.

More work has to be invested in ruling out all spurious effects and artefacts resulting from preparation, radiation damage, and background signal. Sources of artefacts are still many, owing from the still very early stage of the technique. Based on this, it will be of greatest interest to study the onset of what we would call the adult sarcomeric structure, along a maturation of the differentiation pathway. Providing a structural assay and a marker for the 'maturing structure', the presented approach could complement developments of cardiac research and in particular the translational research aming at the development of sarcomere-targeting therapeutics (e.g., acto-myosin modulators).

A second line of research to be exploited is to track down the surprisingly high inter-cell structural variability. Here we would like to understand how local structural changes relate to functions in cardiac tissue, and whether some of these changes could be exploited as structural biomarkers. In this respect, the compatibility

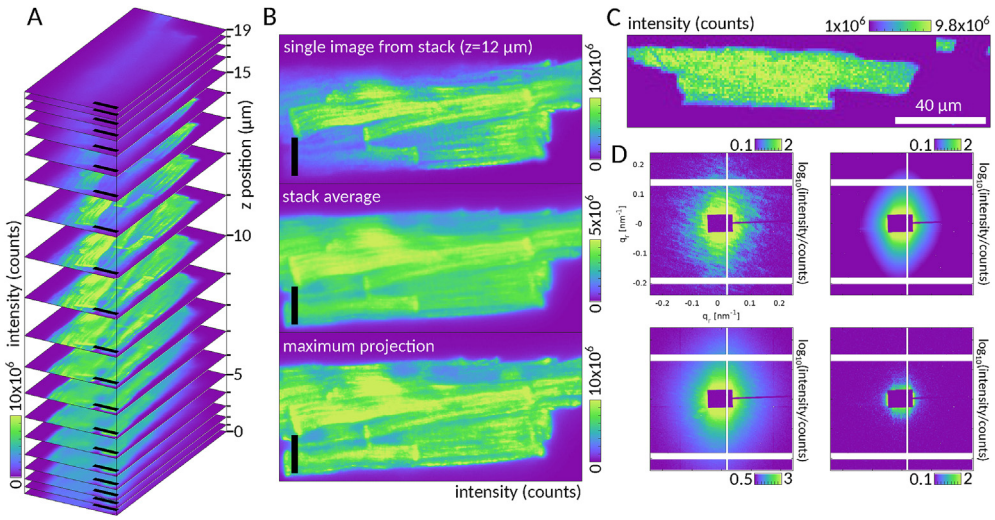

Fig. 8. Correlative microscopy. (A) Confocal stack through freeze-dried cardiomyocytes isolated from an adult mouse heart. The actin cortex was stained with Atto633. The image was recorded using a custom-built STED/confocal microscope that was set-up next to the x-ray beam including a motorized sample translation stage to combine STED or confocal imaging with x-ray diffraction of x-ray holography (Bernhardt et al., 2018). (B) Single image from the stack, stack average and a maximum projection through the entire stack. Since the x-ray darkfield map is sensitive to the projected electron density, we hypothesized that it will most closely resemble the stack average of the confocal stack. (C) Darkfield map of the cell shown in (B). All cellular components add to the signal and the filament structure is washed out. The presence of the myofibrils can be derived from from the anisotropy of the scattering. See (D) for an isolated diffraction pattern (D, top-left), the average (D,top-right), and the maximum projection (D,bottom-left). For completeness, the background intensity is shown in (D, bottom-right).

Table 5
Experimental configuration of beamline P10/GINIX, DESY during confocal fluorescence microscopy and scanning diffraction experiments on freeze-dried cardiac muscle cells.

Beamline	P10 (DESY)
Energy (keV)	8.0
Monochromator	Si(111) channel-cut mono.
Detector	Eiger 4M
Detector distance (m)	5.12
Focus (nm^2)	150 × 150
Focusing	Kirkpatrick-Baez mirrors
I_0 (ph/s)	8.86×10^{11}
Beamstop (mm^2)	17 × 12, 0.28 mm thick Si foil 8 × 7, 0.025 mm thick W foil

of diffraction with screening a large number of cells, much in excess of what can be performed by electron microscopy, is encouraging. However, scaling of throughput will require more work on sample delivery techniques, and more specialized beamline endstations.

One must keep in mind that biological samples suffer from rather stringent radiation damage constraints. For this reason, we found it necessary in this study to sacrifice spatial resolution and use only moderate x-ray focusing to micrometer spot sizes. For future experiments, the selection of scan parameters to optimize the 'quality' of the diffraction signal, has to be drawn special attention to. We expect that with moderate focal spot sizes of around 10 μm and lowerbackground levels, achievable by reducing the propagation distance of the x-ray beam through air, higher orders of equatorial reections as well as intense meridional reections such as the M3 reection will become detectable. In addition, the signal-to-noise ratio of the (1,1) reection will increase, and the ratio of the (1,0) and (1,1) reflection intensity could hence be exploited (Matsubara et al., 1989). At the same time, experiments with nanofocused x-ray beams can still be useful, if radiation damage can be mitigated for example by cryogenic fixation. This also prevents the structural artefacts associated with freeze-drying. Scanning microscopy with nanofocused x-rays can help to localize and characterize acto-myosin complexes in non-adult cardiomyocytes attached to a substrate. In this case high lateral resolution in real space is more relevant than in thick adult cardiomyocytes where the structure is (a) more uniform and (b) anyway averaged over a large thickness along the optical axis. On these adult cardiomyocytes, however, alive recordings are possible since the signal level is high. Such measurements would best be performed with beamsizes on the order of the size of a single cardiomyocyte. Based on the homogeneous lattice spacing for a given cell, we expect that the overall structure per cell does not vary significantly and a larger beamsize would therefore not be a limitation, but would reduce radiation damage and help to cover a high number of dispersed cells in a chamber. In summary, micro-focus beams with spot sizes between 10 μm and 100 μm are recommended for structure analysis of tissue, isolated adult cardiomyocytes as well as living cells, while nano-focused x-ray beams can be useful for example to probe the acto-myosin cortex in less uniform cells such as non-adult cardiomyocytes or fibroblasts cells, provided that radiation damage can be mitigated. In addition, correlative microscopy can help in guiding the diffraction experiment. More generally, combining x-ray imaging techniques with super-resolution fluorescence microscopy, provides additional contrast mechanisms which are to date poorly exploited. For x-rays, these contrast mechanisms are all associated with electron density, either its Fourier components (diffraction) or its projection images (coherent imaging, holography). This type of contrast is highly exploited in structural biology, but almost completely absent in cellular biology or biomedical research, except for - well - classical muscle diffraction, as addressed in the beginning of this manuscript.

Acknowledgements

We thank Kristin Müller for help in the preparation of iPS cells at the home institution and the biological laboratories of the synchrotron endstation P10 and the ESRF (Bio-medical Facility), as well as for implementing the micro-patterning technique on silicon nitride substrates. Mike Kanbach has helped in the fabrication of a silicon wafer used for micro-patterning. We are very grateful to

Susanne Hengst for her dedicated help in cell culture and preparation, and Stefan Luther and Marion Kunze of Max Planck Institute for Dynamics and Self-Organization for providing the neonatal rat cardiomyocytes. We also thank Mohamed Belal for the preparation of TAC and sham mice and Alessya Jacqueline Kretzschmar for the extraction of the cardiomyocytes from the hearts. Manfred Burghammer and the team of the Bio-medical facility and the safety group of the ESRF provided an excellent work environment and support during beamtime at ID13. Michael Sprung is gratefully acknowledged for support during beamtimes at beamline P10. We also thank Erik Stellamanns for advice and support in using the biology laboratory and Markus Osterhoff for helpful discussions and the indispensable implementation of the continuous scanning modality at beamline P10 as well as useful tools for online data analysis. We acknowledge SFB937 Collective Behavior of Soft and Biological Matter/Project A11 and Project A18 for funding the research project on cardiac tissue cells, and BMBF/Verbundforschung (project 05K16MG2) for funding instrumentation at the GINIX endstation of the P10 beamline.

References

Ait-Mou, Y., Hsu, K., Farman, G.P., Kumar, M., Greaser, M.L., Irving, T.C., de Tombe, P.P., 2016. Titin strain contributes to the frank-starling law of the heart by structural rearrangements of both thin- and thick-filament proteins. Proc. Natl. Acad. Sci. Unit. States Am. 113 (8), 2306–2311.

Bernhardt, M., Priebe, M., Osterhoff, M., Wollnik, C., Diaz, A., Salditt, T., Rehfeldt, F., 2016. X-ray micro- and nanodiffraction imaging on human mesenchymal stem cells and differentiated cells. Biophys. J. 110 (3), 680–690.

Bernhardt, M., Nicolas, J.-D., Eckermann, M., Eltzner, B., Rehfeldt, F., Salditt, T., 2017. Anisotropic x-ray scattering and orientation fields in cardiac tissue cells. N. J. Phys. 19 (1), 013012.

Bernhardt, M., Nicolas, J.-D., Osterhoff, M., Mittelstädt, H., Reuss, M., Harke, B., Wittmeier, A., Sprung, M., Köster, S., Salditt, T., 2018. Combined hard x-ray and sted microscopy of cardiac tissue cells. submitted for publication.

Chen, S., Deng, J., Yuan, Y., Flachenecker, C., Mak, R., Hornberger, B., Jin, Q., Shu, D., Lai, B., Maser, J., Roehrig, C., Paunesku, T., Gleber, S.C., Vine, D.J., Finney, L., VonOsinski, J., Bolbat, M., Spink, I., Chen, Z., Steele, J., Trapp, D., Irwin, J., Feser, M., Snyder, E., Brister, K., Jacobsen, C., Woloschak, G., Vogt, S., 2014. The Bionanoprobe: hard X-ray fluorescence nanoprobe with cryogenic capabilities. J. Synchrotron Radiat. 21 (1), 66–75.

de Jonge, M.D., Ryan, C.G., Jacobsen, C.J., 2014. X-ray nanoprobes and diffraction-limited storage rings: opportunities and challenges of fluorescence tomography of biological specimens. J. Synchrotron Radiat. 21 (5), 1031–1047.

deAlmeida, A.C., van Oort, R.J., Wehrens, X.H.T., 2010. Transverse aortic constriction in mice. J. Visualized Exp. (38), e1729.

Denz, M., Brehm, G., Hémonnot, C.Y.J., Spears, H., Wittmeier, A., Cassini, C., Saldanha, O., Perego, E., Diaz, A., Burghammer, M., Köster, S., 2018. Cyclic olefin copolymer as an x-ray compatible material for microfluidic devices. Lab a Chip 18, 171–178.

Ekeberg, T., Svenda, M., Abergel, C., Maia, F.R.N.C., Seltzer, V., Claverie, J.-M., Hantke, M., Jönsson, O., Nettelblad, C., van der Schot, G., Liang, M., DePonte, D.P., Barty, A., Seibert, M.M., Iwan, B., Andersson, I., Loh, N.D., Martin, A.V., Chapman, H., Bostedt, C., Bozek, J.D., Ferguson, K.R., Krzywinski, J., Epp, S.W., Rolles, D., Rudenko, A., Hartmann, R., Kimmel, N., Hajdu, J., 2015. Three-dimensional reconstruction of the giant mimivirus particle with an x-ray free-electron laser. Phys. Rev. Lett. 114, 098102.

Fratzl, P., Weinkamer, R., 2007. Natures hierarchical materials. Prog. Mater. Sci. 52 (8), 1263–1334.

Ghazal, A., Lafleur, J.P., Mortensen, K., Kutter, J.P., Arleth, L., Jensen, G.V., 2016. Recent advances in x-ray compatible microfluidics for applications in soft materials and life sciences. Lab a Chip 16, 4263–4295.

Hantke, M.F., Hasse, D., Maia, F.R.N.C., Ekeberg, T., John, K., Svenda, M., Loh, N.D., Martin, A.V., Timneanu, N., Larsson, D.S.D., van der Schot, G., Carlsson, G.H., Ingelman, M., Andreasson, J., Westphal, D., Liang, M., Stellato, F., DePonte, D.P., Hartmann, R., Kimmel, N., Kirian, R.A., Seibert, M.M., Mühlig, K., Schorb, S., Ferguson, K., Bostedt, C., Carron, S., Bozek, J.D., Rolles, D., Rudenko, A., Epp, S., Chapman, H.N., Barty, A., Hajdu, J., Andersson, I., 2014. High-throughput imaging of heterogeneous cell organelles with an x-ray laser. Nat. Photon. 8, 943.

Hémonnot, C.Y.J., Köster, S., 2017. Imaging of biological materials and cells by x-ray scattering and diffraction. ACS Nano 11 (9), 8542–8559.

Hitchcock, A.P., 2015. Soft x-ray spectromicroscopy and ptychography. J. Electron. Spectrosc. Relat. Phenom. 200, 49–63.

Huxley, H.E., 1996. A personal view of muscle and motility mechanisms. Annu. Rev. Physiol. 58, 1–19.

Irving, T.C., Konhilas, J., Perry, D., Fischetti, R., de Tombe, P.P., 2000. Myofilament lattice spacing as a function of sarcomere length in isolated rat myocardium. Am. J. Physiol. Heart Circ. Physiol. 279 (5), 2568–2573.

Karlsson, U., Schultz, R.L., 1965. Fixation of the central nervous system for electron microscopy by aldehyde perfusion: I. preservation with aldehyde perfusates versus direct perfusion with osmium tetroxide with special reference to membranes and the extracellular space. J. Ultra. Res. 12 (1), 160–186.

Kimura, T., Joti, Y., Shibuya, A., Song, C., Kim, S., Tono, K., Yabashi, M., Tamakoshi, M., Moriya, T., Oshima, T., Ishikawa, T., Bessho, Y., Nishino, Y., 2014. Imaging live cell in micro-liquid enclosure by x-ray laser diffraction. Nat. Commun. 5, 3052.

Kovesi, P., 2018. Good colour maps: How to design them. ArXiv e-prints.

Lichtenegger, H., Müller, M., Paris, O., Riekel, C., Fratzl, P., 1999. Imaging of the helical arrangement of cellulose fibrils in wood by synchrotron X-ray microdiffraction. J. Appl. Crystallogr. 32 (6), 1127–1133.

Linari, M., Brunello, E., Reconditi, M., Fusi, L., Caremani, M., Narayanan, T., Piazzesi, G., Lombardi, V., Irving, M., 2015. Force generation by skeletal muscle is controlled by mechanosensing in myosin filaments. Nature 528 (7581), 276–279.

Lombardi, V., Piazzesi, G., Reconditi, M., Linari, M., Lucii, L., Stewart, A., Sun, Y.-B., Boesecke, P., Narayanan, T., Irving, T., Irving, M., 2004. X-ray diffraction studies of the contractile mechanism in single muscle fibres. Phil. Trans.: Biol. Sci. 359 (1452), 1883–1893.

Lutz-Bueno, V., Zhao, J., Mezzenga, R., Pfohl, T., Fischer, P., Liebi, M., 2016. Scanning-saxs of microfluidic flows: nanostructural mapping of soft matter. Lab a Chip 16, 4028–4035.

Matsubara, I., 1980. X-ray diffraction studies of the heart. Annu. Rev. Biophys. Bioeng. 9 (1), 81–105.

Matsubara, I., Maughan, D.W., Saeki, Y., Yagi, N., 1989. Cross-bridge movement in rat cardiac muscle as a function of calcium concentration. J. Physiol. 417 (1), 555–565.

McDevitt, T.C., Angello, J.C., Whitney, M.L., Reinecke, H., Hauschka, S.D., Murry, C.E., Stayton, P.S., 2002. In vitro generation of differentiated cardiac myofibers on micropatterned laminin surfaces. J. Biomed. Mater. Res. 60, 472–479.

Meisburger, S., Warkentin, M., Chen, H., Hopkins, J., Gillilan, R., Pollack, L., Thorne, R., 2013. Breaking the radiation damage limit with cryo-saxs. Biophys. J. 104 (1), 227–236.

Nakasako, M., Takayama, Y., Oroguchi, T., Sekiguchi, Y., Kobayashi, A., Shirahama, K., Yamamoto, M., Hikima, T., Yonekura, K., Maki-Yonekura, S., Kohmura, Y., Inubushi, Y., Takahashi, Y., Suzuki, A., Matsunaga, S., Inui, Y., Tono, K., Kameshima, T., Joti, Y. Hoshi, T., Kotobuki-1 apparatus for cryogenic coherent x-ray diffraction imaging, Rev. Sci. Instrum. 84 (9).

Nicolas, J.-D., Bernhardt, M., Krenkel, M., Richter, C., Luther, S., Salditt, T., 2017. Combined scanning X-ray diffraction and holographic imaging of cardiomyocytes. J. Appl. Crystallogr. 50 (2), 612–620.

Nicolas, J.-D., Bernhardt, M., Markus, A., Alves, F., Burghammer, M., Salditt, T., 2017. Scanning X-ray diffraction on cardiac tissue: automatized data analysis and processing. J. Synchrotron Radiat. 24 (6), 1163–1172.

Priebe, M., Bernhardt, M., Blum, C., Tarantola, M., Bodenschatz, E., Salditt, T., 2014. Scanning x-ray nanodiffraction on dictyostelium discoideum. Biophys. J. 107 (11), 2662–2673.

Reconditi, M., Caremani, M., Pinzauti, F., Powers, J.D., Narayanan, T., Stienen, G.J.M., Linari, M., Lombardi, V., Piazzesi, G., 2017. Myosin filament activation in the heart is tuned to the mechanical task. Proc. Natl. Acad. Sci. Unit. States Am. 114 (12), 3240–3245.

Richter, C., Christoph, J., Lehnart, S.E., Luther, S., 2016. Optogenetic Light Crafting Tools for the Control of Cardiac Arrhythmias. Springer, New York, pp. 293–302.

Rother, J., Richter, C., Turco, L., Knoch, F., Mey, I., Luther, S., Janshoff, A., Bodenschatz, E., Tarantola, M., 2015. Crosstalk of cardiomyocytes and fibroblasts in co-cultures. Open Biol. 5 (6), 150038.

Sakdinawat, A., Attwood, D., 2010. Nanoscale x-ray imaging. Nat. Photon. 4 (12), 840–848.

Schultz, R.L., Karlsson, U., 1965. Fixation of the central nervous system for electron microscopy by aldehyde perfusion: ii. effect of osmolarity, ph of perfusate, and fixative concentration. J. Ultra. Res. 12 (1), 187–206.

Seibert, M.M., Boutet, S., Svenda, M., Ekeberg, T., Maia, F.R.N.C., Bogan, M.J., TÂ®mneanu, N., Barty, A., Hau-Riege, S., Caleman, C., Frank, M., Benner, H., Lee, J.Y., Marchesini, S., Shaevitz, J.W., Fletcher, D.A., Bajt, S., Andersson, I., Chapman, H.N., Hajdu, J., 2010. Femtosecond diffractive imaging of biological cells. J. Phys. B Atom. Mol. Opt. Phys. 43 (19), 194015.

Shen, K., Qi, J., Kam, L.C., 2008. Microcontact printing of proteins for cell biology. J. Visualized Exp. 1–3.

Strelnikova, N., Sauter, N., Guizar-Sicairos, M., Göllner, M., Diaz, A., Delivani, P., Chacón, M., Tolić, I.M., Zaburdaev, V., Pfohl, T., 2017. Live cell x-ray imaging of autophagic vacuoles formation and chromatin dynamics in fission yeast. Sci. Rep. 7 (1), 13775.

Tiburcy, M., Didié, M., Boy, O., Christalla, P., Döker, S., Naito, H., Karikkineth, B.C., El-Armouche, A., Grimm, M., Nose, M., Eschenhagen, T., Zieseniss, A., Katschinski, D.M., Hamdani, N., Linke, W.A., Yin, X., Mayr, M., Zimmermann, W.-H., 2011. Terminal differentiation, advanced organotypic maturation, and modeling of hypertrophic growth in engineered heart tissuenovelty and significance. Circ. Res. 109 (10), 1105–1114.

Tiburcy, M., Hudson, J.E., Balfanz, P., Schlick, S., Meyer, T., Chang Liao, M.-L., Levent, E., Raad, F., Zeidler, S., Wingender, E., Riegler, J., Wang, M., Gold, J.D., Kehat, I., Wettwer, E., Ravens, U., Dierickx, P., van Laake, L.W., Goumans, M.J., Khadjeh, S., Toischer, K., Hasenfuss, G., Couture, L.A., Unger, A., Linke, W.A., Araki, T., Neel, B., Keller, G., Gepstein, L., Wu, J.C., Zimmermann, W.-H., 2017. Defined engineered human myocardium with advanced maturation for applications in heart failure modeling and repairclinical perspective. Circulation 135

(19), 1832–1847.
Toischer, K., Rokita, A.G., Unsöld, B., Zhu, W., Kararigas, G., Sossalla, S., Reuter, S.P., Becker, A., Teucher, N., Seidler, T., Grebe, C., Preuß, L., Gupta, S.N., Schmidt, K., Lehnart, S.E., Krüger, M., Linke, W.A., Backs, J., Regitz-Zagrosek, V., Schäfer, K., Field, L.J., Maier, L.S., Hasenfuss, G., 2010. Differential cardiac remodeling in preload versus afterload. Circulation 122 (10), 993–1003.
van der Schot, G., Svenda, M., Maia, F.R.N.C., Hantke, M., DePonte, D.P., Seibert, M.M., Aquila, A., Schulz, J., Kirian, R., Liang, M., Stellato, F., Iwan, B., Andreasson, J., Timneanu, N., Westphal, D., Almeida, F.N., Odic, D., Hasse, D., Carlsson, G.H., Larsson, D.S.D., Barty, A., Martin, A.V., Schorb, S., Bostedt, C., Bozek, J.D., Rolles, D., Rudenko, A., Epp, S., Foucar, L., Rudek, B., Hartmann, R., Kimmel, N., Holl, P., Englert, L., Duane Loh, N.-T., Chapman, H.N., Andersson, I., Hajdu, J., Ekeberg, T., 2015. Imaging single cells in a beam of live cyanobacteria with an x-ray laser. Nat. Commun. 6, 5704.
Weinhausen, B., Nolting, J.-F., Olendrowitz, C., Langfahl-Klabes, J., Reynolds, M., Salditt, T., Köster, S., 2012. X-ray nano-diffraction on cytoskeletal networks. N. J. Phys. 14 (8), 085013.
Weinhausen, B., Saldanha, O., Wilke, R.N., Dammann, C., Priebe, M., Burghammer, M., Sprung, M., Köster, S., 2014. Scanning x-ray nanodiffraction on living eukaryotic cells in microfluidic environments. Phys. Rev. Lett. 112, 088102.
Wilke, R.N., Priebe, M., Bartels, M., Giewekemeyer, K., Diaz, A., Karvinen, P., Salditt, T., 2012. Hard x-ray imaging of bacterial cells: nano-diffraction and ptychographic reconstruction. Optic Express 20 (17), 19232–19254.
Yusuf, M., Zhang, F., Chen, B., Bhartiya, A., Cunnea, K., Wagner, U., Cacho-Nerin, F., Schwenke, J., Robinson, I.K., 2017. Procedures for cryogenic X-ray ptychographic imaging of biological samples. IUCrJ 4 (2).